Hindawi
Advances in Civil Engineering
Volume 2021, Article ID 8949846, 16 pages
https://doi.org/10.1155/2021/8949846

Research Article

Mechanism and Stability Analysis of Deformation Failure of a Slope

Yingfa Lu,[1] **Gan Liu**,[1] **Kai Cui**,[2] **and Jie Zheng**[3]

[1]*School of Civil Engineering and Resource Environment, Hubei University of Technology, Wuhan, Hubei, China*
[2]*Key Laboratory of High-Speed Railway Engineering of the Ministry of Education, Southwest Jiaotong University, Chengdu, Sichuan, China*
[3]*Zhengzhou Highway Development Center, Zhengzhou, Henan, China*

Correspondence should be addressed to Yingfa Lu; 20121063@hbut.edu.cn

Received 19 May 2021; Revised 19 June 2021; Accepted 31 July 2021; Published 27 August 2021

Academic Editor: Guang-Liang Feng

Force distribution during progressive slope failure is an important element in slope stability analysis. In this study, five mechanical failure modes are proposed for thrust- and pull-type slopes, respectively, and five field forms of thrust-type slopes are described. The properties of progressive failure are evaluated quantitatively: the failure mode of slope obeys the geo-material rule under the peak stress state, and the instability range is gradually developed. The critical stress state zone is in the process of dynamic change with the development of deformation. It appears that the driving sliding force is greater than the frictional resistance along the sliding surface. When rock or soil stabilizing stresses are at maximum, the vector sum of the driving sliding stress and stabilizing stress is equal to zero at the critical state. The frictional resistance is equal to the driving sliding force in the stable and less-stable regions, and the normal pressure is wherever equal to the counterpressure. Rigid, flexible, and rigid-flexible design theories are proposed for slope control. New terms are defined and used to evaluate the stability. The conventional local and surplus stability factors of slopes and their calculation are explained. The force distribution rule is analyzed during progressive failure, and the conventional stability factor definition is discussed. The geological settings and monitoring data of landslides are used to analyse changes in the critical stress state. An example is given to illustrate the failure process analysis. The results show that progressive failure can be well represented and the safety factor can be well described by the main thrust method (MTM), comprehensive displacement method (CDM), and surplus displacement method (SDM), which can be used to feasibly evaluate slope stability.

1. Introduction

The slope failure mechanism and stability analysis are traditional topics in geotechnical engineering. Geotechnical disasters such as landslide, collapse, rockburst, and water inrush have occurred frequently in recent years [1, 2]. More than ten sort of limit equilibrium stability calculation methods for slope were given in previous studies, such as the Fellenius method [3], the simplified Bishop method [4], the Spencer method [5], the Janbu method [6], the Sarma method [7], the wedge method, and the finite element strength reduction method (SRM) [8–11]. In traditional slope stability analyses, the limit equilibrium slice method is the most often used [12–18]. For the slope with a given slip surface to be statically analyzed, different limit equilibrium slice methods have different assumptions about the action point of the force on the bottom edge of the slice and the direction and action line of thrust between the slices. With the development of numerical analysis, more and more scholars have begun to try other calculation methods, such as chart-based slope stability assessment using the generalized Hoek–Brown criterion and extremum solutions to the limit equilibrium method subjected to physical admissibility [19–31]. Other researchers established a three-dimensional strict equilibrium equation based on certain assumptions and proposed four criteria: potential sliding surface minimum parameter value criterion, slope active reinforcement force upper limit criterion, lower limit criterion for

sliding surface, and sliding and upper bound criterion for potential sliding surface selection [32].

The finite element method is the most widely used numerical analysis method in geotechnical engineering. In the field of slope analysis, the main software packages with strong functionality and wide application are ABAQUS, ANASYS, GeoStudio, rational infiltration analysis, etc. The corresponding analysis method is based on small deformation assumption and is usually applied to continuum mechanics media. Other numerical methods such as the fast Lagrangian analysis of continua (FLAC) method, discrete element method, discontinuous deformation analysis (DDA) method, and popular element method have been increasingly applied to landslide stability analysis.

The above landslide stability analysis is based on the limit equilibrium state. However, landslide damage is a process of gradual development [33–40]. That is, some zones are in the postfailure stress state, some zones are in the critical stress state, some zones are in the prepeak stress state [41, 42], and some zones are in the small deformation state, and this evolution process changes with changes in the environment. However, the traditional method does not consider the nonuniform distribution of the driving force along the sliding surface; different numerical analysis methods have certain difficulties in dealing with the discontinuous surface. Therefore, this paper proposes a new analytical method to solve the above problems.

In this paper, the sliding surface is divided into an unstable zone, a critical zone, a less-stable zone, and a stable zone. The transfer law of the landslide force is analyzed, and the characteristics of the critical block (or unit) force of the slope are proposed. The failure mechanisms, natures, and destruction control standards of thrust-type, pull-type, and mixed landslides are described. Based on the deformation and stress analysis, combined with the possible failure modes of slope, the following methods are defined: comprehensive sliding-resistance, main thrust, comprehensive displacement, and surplus displacement methods. The above analysis methods can be used to analyse slope progressive failure stability and provide a new idea for the study of landslide stability.

2. Failure Modes

Landslides occur due to long-term geological processes, environmental factors, human engineering, etc. Few studies have focused on the progressive deformation process from the initiation crack to the failure of landslide. In this paper, the whole failure process of the landslide can be described by the different stress distribution characteristics of sliding surface points. Only one point along the sliding surface is in the critical state when the sliding force is equal to the sliding resistance for a 2D landslide, and this stress distribution is defined as the critical state. The remaining points are in the postfailure stress state, and their sliding force is greater than the antisliding force; the landslide is in a state of "mechanical failure" at this moment. In the following, the deformation mechanism, failure modes, and destruction control standards are analyzed from a mechanical viewpoint.

2.1. Thrust-Type Landslide. The deformation and force transfer of landslides are established based on the fundamental mechanical behaviours of geomaterials. The load-displacement characteristics of rock and soil can be presented as types I and III curves (Figure 1); any point on the sliding surface experiences elastic stress, elastoplastic stress, critical stress, postfailure stress, and residual stress states from the initiation to the mechanical failure of the slope. At a certain moment, points a_1, a_2, a_3, and a_4 correspond to the postfailure stress state; point a_4 to the critical stress; points a_5 and a_6 to the elastoplastic stress state; and point a_7 to the elastic stress state in a 2D landslide problem. The postfailure stress state can be defined as an unstable zone, the critical stress state as a critical zone, the elastoplastic stress state as a less-stable zone, and the elastic stress state as a stable zone (Figure 1).

The failure occurs along the soft interlayer $(a_1, \ldots, a_5, \ldots, a_8)$, which is defined as mode I. In the rear part, the failure occurs along the weak intercalation $(a_1, \ldots, a_5)$ and along the sliding body (a_5, a_9) in the front part of the landslide, which is classified as mode II. The failure modes are controlled by the mechanical behaviours of soils/rocks.

2.2. Pull-Type Landslide. At a certain moment, points (b_1, b_2) correspond to the postfailure stress state and point (b_3) corresponds to the critical stress state. Points $(b_4, b_5, b_6$ or $b_7, b_8, b_9)$ are before the peak stress, and the whole sliding surface can be classified into unstable, critical, less-stable, and stable zones (Figure 2). The failure occurs along the soft interlayer $(b_1, \ldots, b_6)$, which is defined as mode I. In the front part, the failure occurs along the weak intercalation (b_1, b_2, b_3) and failure occurs along the sliding body (b_7, b_8, b_9) in the rear part of the landslide, which is classified as mode II. In the front part, failure occurs along the weak intercalation (b_1, b_2, b_3) and along the section of the sliding body (b_3, b_{12}) as traction strength control, which is defined as mode III. The failure modes are also controlled by the mechanical behaviours of soils/rocks.

2.3. Mixed Failure Mode. The thrust- and pull-types are the main failure modes during the progressive deformation process of landslides. However, a mixed failure mode of thrust- and pull-types can take place. For instance, tensile-shear failure occurs at depth (see Figure 3, point c_4), while the tensile stress increases to its strength. Traction failure (σ_n) occurs along section (c_4c_8). The first scarp is formed. If the tensile strength does not reach its strength, this scarp does not develop, and a pull-type landslide is certainly produced in zone $(c_4c_8c_9c_1c_2c_3c_4)$. When the tensile stress reaches the tensile strength value, the second scarp (c_9c_3) forms; the segment $(c_5c_4c_3)$ is in a postfailure stress state, and a corresponding unbalanced (or driving sliding) force is shown. The sliding body $(c_3c_4c_5c_6c_7c_8c_9c_3)$ exhibits thrust-type characteristics, and the driving sliding force impels the sliding body ahead. Two unstable, critical, less-stable, and stable zones appear during this period of landslide deformation. When the critical state disappears in the $c_9c_1c_2c_3c_9$ zone, the thrust-type feature is shown for the whole landslide (Figure 3).

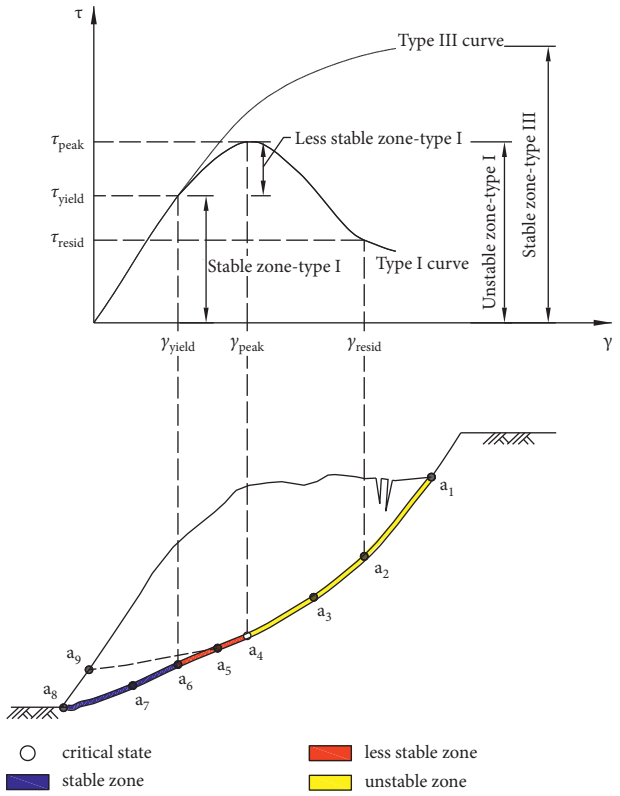

Figure 1: Failure modes of thrust-type landslides.

At a certain moment, points (b_1, b_2) correspond to the postfailure stress state and point (b_3) corresponds to the critical stress state; points $(b_4, b_5, b_6$ or $b_7, b_8, b_9)$ are before the peak stress, and the whole sliding face can be classified into unstable, critical, less-stable, and stable zones (Figure 2). The failure occurs along the soft interlayer $(b_1, \ldots, b_6)$, which is defined as mode I. In the front part, failure occurs along the weak intercalation (b_1, b_2, b_3), and failure occurs along the sliding body (b_7, b_8, b_9) in the rear.

The second mixed failure mode is often involved in a landslide with progressive deformation. At first, the landslide initiates in the rear and front parts of the landslide body along the sliding face, and the postfailure stress state corresponds to the rear and front parts. A thrust- ($d_1 d_2$ zone) and pull- ($d_6 d_5$ zone) type landslide are present in the rear and front parts on the sliding surface, respectively. An antisliding feature takes place in the middle part ($d_2 d_3 d_4 d_5$ zone). Two unstable, critical, less-stable, and stable zones appear during the progressive deformation process (Figure 4). With time and the development of deformation, the antisliding area decreases and the failure area increases. Finally, only one point corresponds to the critical state, and the whole landslide is at the point of "mechanical failure." The landslide initiates at the front, rear, or middle part of the landslide along the sliding face, which can be defined the "mixed failure mode."

3. Failure Process Analysis

The failure mode of the slope on the sliding surface point obeys the mechanical rule of rock and soil mass during the development of progressive deformation, and the mechanical failure properties of the two different types of slopes are analyzed.

3.1. Characteristics of the Thrust-Type Slope. A continuous shear failure occurs from the rear (see Figure 5, point *A*) to the front (see Figure 5, point *C*) (or from point *G* to *Q* of the soft interlayer) regions of a thrust-type slope during the development of progressive deformation. The stress at the failure point is in the peak state; the elastoplastic stress state is located in front of the failure point; and the postfailure stress state is behind the failure point (Figure 5). This failure mode is defined as mode I, and a shear failure occurs along the entire sliding surface. Tensile or tensile-shear failure occurs in the rear zone (see Figure 5, *DB*), and shear failure occurs in the front zone (see Figure 5, *BC*). Then, possible shear failure occurs in the *ABD* triangular area, which can be defined as mode II. In mode III, shear failure occurs in the rear zone (see Figure 5, *ABE*) and tensile (or tensile-shear) failure occurs in the front zone (see Figure 5, *EF*). Mode IV is a combination of modes II and III, in which failure occurs in the rear zone by tensile (or tensile-shear) failure, in the middle zone by shear failure, and in the front zone by tensile (or tensile-shear) failure (see Figure 5, DBEF). Mode V corresponds to a rock mass with distributed joints (or fissures), and shear, tensile, and tensile-shear failures occur along the soft interlayer and joints (or fissures) (see Figure 5, *GHIJ*. . .*KLMP*) alternately. The stability classification (stable zone, less-stable zone, critical zone, and unstable zone; Figure 1) along the entire sliding surface applies for the five failure modes of a thrust-type slope.

3.2. Characteristics of a Pull-Type Slope. Shear failure occurs from the front (see Figure 6, point *B*) to the rear (see Figure 6, point *A*) regions of a pull-type slope during the development of progressive deformation. The stress at the failure point is in the peak state; the elastoplastic stress state is behind the failure point; and the postfailure stress state is in front of the failure point. This failure mode is defined as mode I. Tensile or tensile-shear failure occurs in the rear zone (see Figure 6, *DC*), and shear failure occurs in the front zone (see Figure 6, *CB*). Then, possible shear failure occurs in the *ACD* triangular area, which can be defined as mode II. In mode III, shear failure occurs in the front zone and tensile failure occurs in the rear zone of the sliding body (see Figure 6, *EF*). Mode IV corresponds to a rock mass with distributed joints (or fissures): shear, tensile, and shear failures occur along the soft interlayer and joints (or fissures) alternately (see Figure 6, *GHIJ*. . .*KLMP*). Mode V corresponds to a combination of mode IV and a shear failure (or tensile-shear or tensile failure (see Figure 6, *ET*, or *ES*, or *EF*)) of the sliding body. The previous peak stress state is behind the zone, and the postfailure state is in front of the zone corresponding to a critical state for the five mechanical failure modes of the pull-type slope.

3.3. Characteristics of Deformation. Generally, a slope consists of a sliding body, sliding surface, and landslip bed.

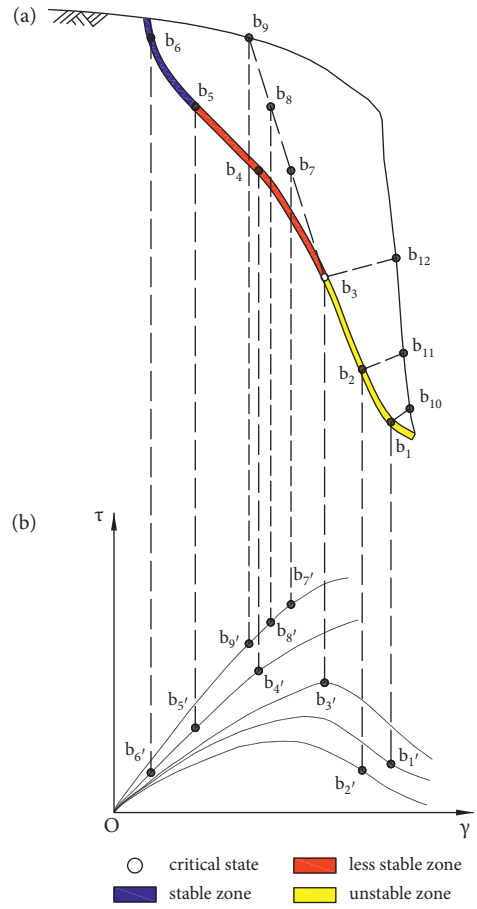

Figure 2: Failure modes of pull-type landslides.

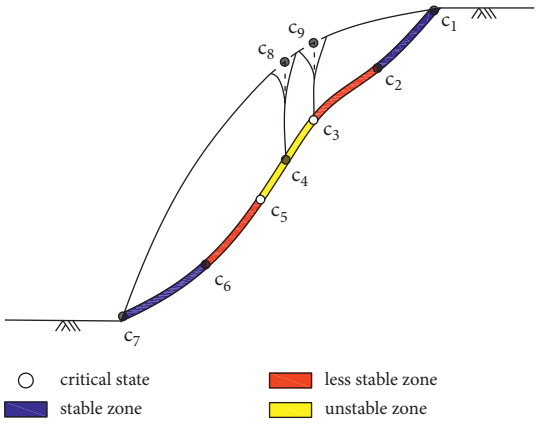

Figure 3: Failure mode of initiation in the middle part of the sliding face.

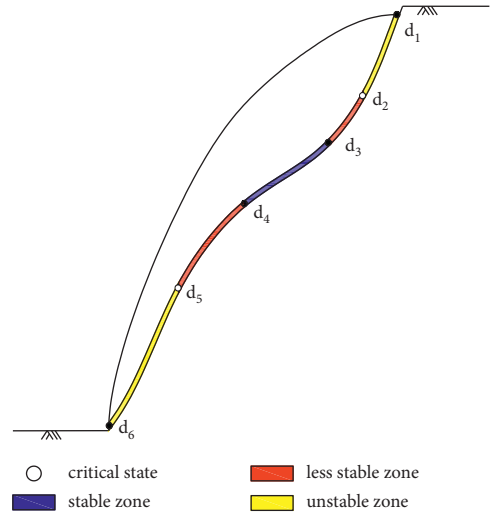

Figure 4: Failure of initiation on the front and rear part of the sliding face.

The values of the shear and tensile strengths of the sliding surface, sliding body, and landslip bed follow a small, moderate, and large pattern. At first, the failure of the sliding surface occurs and the deformation of the sliding body produces a sliding surface. The stress state of the sliding surface changes with the development of deformation. The characteristics of the complete stress-strain process are presented by each point on the sliding surface. The elastic, elastoplastic, peak, postfailure, and residual stress states are shown by each point on the sliding surface during the progressive failure process. The five different stress states may be represented by the points on the sliding surface at the same time. The driving sliding force on the sliding surface is

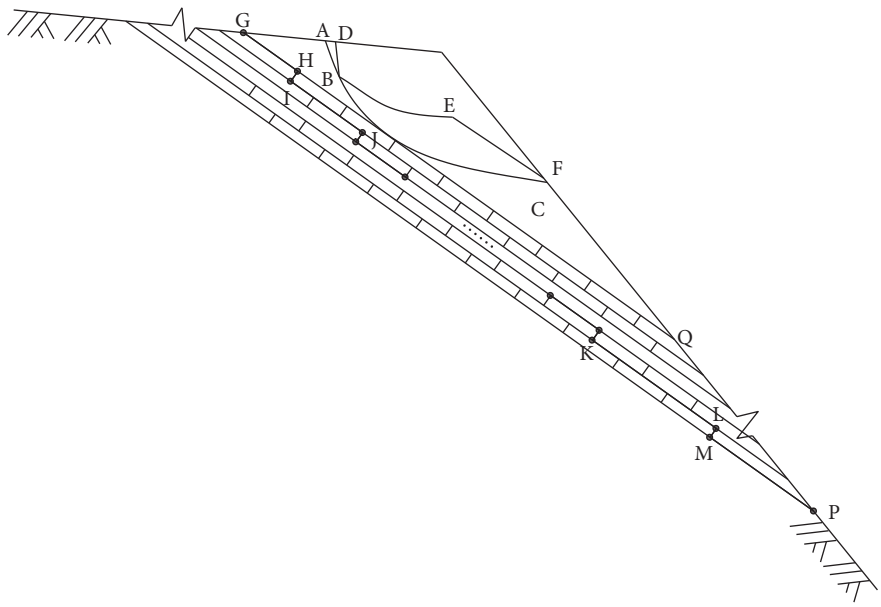

Figure 5: The five failure modes of a thrust-type slope.

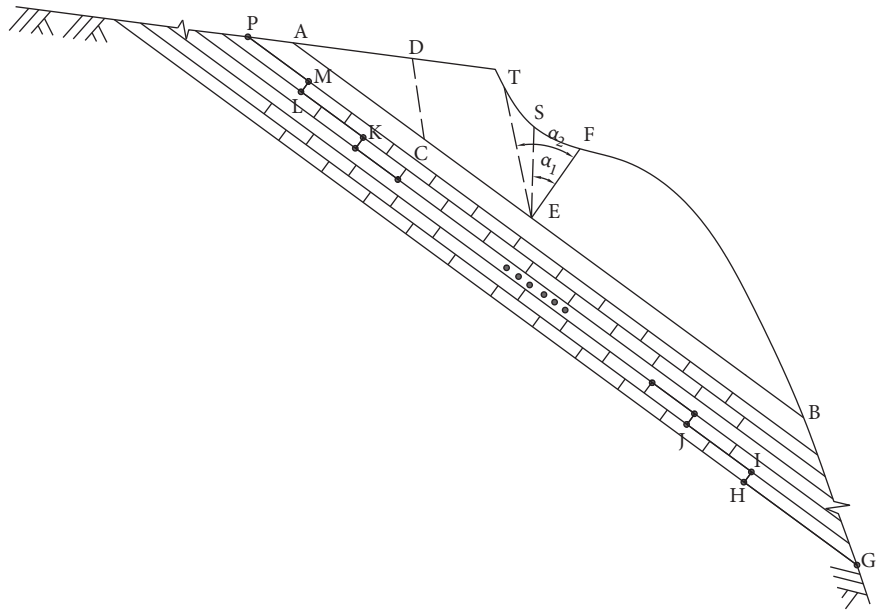

Figure 6: The five failure modes of a pull-type slope.

greater than the frictional resistance in the postfailure zone. Certainly, an unbalanced thrust exists for a slope along the sliding surface. In the front zone of the sliding surface, the driving sliding force is equal to the frictional resistance on the sliding surface and a surplus frictional resistance corresponding to the strength existing for the thrust-type slope. Thrust-type slopes in the field exhibit five forms. In form I, the elastic stress state covers the entire sliding surface. In form II, the whole sliding surface is in the stress state before the peak stress. In form III, a zone of the sliding surface is in the previous peak stress state, another zone is in the critical stress state, and the remainder of the sliding surface is in the postfailure and residual stress states. In form IV, the entire sliding surface is in the postfailure and residual stress states. In form V, only the residual stress state is present for the entire sliding surface (Figure 7). Form I cannot significantly perform slope control without additional reinforcement. The critical state is often the peak stress state for form II, and whether the slope controls are performed depends on the human influence. The critical state does not necessarily correspond to the peak stress for forms III, IV, and V, but the critical state exists for thrust-type slopes. Large deformation is produced for these three slopes. The geometric shape after deformation may possibly be favourable to thrust-type slope

stability, but performing slope control is necessary if the effects on humans are important.

4. Force Distribution on the Sliding Surface

In this section, the different failure modes are introduced during the progressive deformation process and the force distribution properties on the sliding surface are explained taking the thrust-type slope as an example.

An element (Figure 8) considered to represent the stress state of the sliding surface, where $\sigma_n^u, \sigma_\tau^u$, and σ_θ^u are the stresses from the sliding force of the sliding body and ${\sigma_n}^b, {\sigma_\tau}^b$, and ${\sigma_\theta}^b$ are the frictional stresses from the landslip bed. The driving shear stresses are greater than the frictional shear stresses in the postfailure zone along the sliding surface. The frictional shear stress reaches a maximum, and the driving shear stresses are equal to the frictional shear stresses at the critical state. The frictional shear stresses are equal to the driving shear stress in the front zone, corresponding to the critical state. But, the frictional shear stresses do not reach their maximum; the normal stress is equal to the counterstress in the whole sliding surface. The shear displacement is discontinuous in the postfailure zone; both shear stress and shear strain in the postfailure zone on the sliding surface are clearly discontinuous and present a challenge for numerical analysis. Certainly, the driving sliding force (P_i) and pressure (N_i) result from the sliding bed; the frictional force (F_i) and counterpressure (N_i^f) proceed from the landslip bed (Figure 9) for a two-dimensional thrust-type slope. The driving sliding force is greater than the frictional resistance in the postfailure zone on the sliding surface, and the driving sliding force is equal to the frictional resistance in the other zones. However, the maximum frictional resistance is reached at the critical state, when the pressure is equal to the counterpressure on the whole sliding surface.

5. Critical State

The slope stability is related to the critical state. The critical state is an obstacle to unstable zone development. Three stress balance equations exist at the critical state for numerical analysis on the sliding surface:

$$\begin{aligned} \left|\sigma_\theta^u\right| &= \left|\sigma_\theta^b\right|, \\ \left|\sigma_\tau^u\right| &= \left|\sigma_\tau^b\right|, \\ \left|\sigma_n^u\right| &= \left|\sigma_n^b\right|. \end{aligned} \tag{1}$$

The force balance equations in the X-, Y-, and Z-axial directions at the critical state must be satisfied for the slice block method under the shear failure condition:

$$\begin{aligned} \sum F_x &= 0, \\ \sum F_y &= 0, \\ \sum F_z &= 0. \end{aligned} \tag{2}$$

The moment balance equations in the XY-, YZ-, and ZX-planes of the critical state must exist for the slice block method under failure conditions:

$$\begin{aligned} \sum M_{xy} &= 0, \\ \sum M_{yz} &= 0, \\ \sum M_{zx} &= 0. \end{aligned} \tag{3}$$

By considering the field state, the combination of equations (2) and (3) may be chosen for the slice block method. For instance, the moment balance equation is satisfied in the XY-plane and the force balance equations exist in the X-, Y-, and Z-axial directions at the critical state for the slice block method:

$$\begin{aligned} XY - \text{plane} &: \sum M_{xy} = 0, \\ X - \text{axial direction} &: \sum F_x = 0, \\ Y - \text{axial direction} &: \sum F_y = 0, \\ Z - \text{axial direction} &: \sum F_z = 0. \end{aligned} \tag{4}$$

When tensile and shear failures occur for the same slice block, the tensile and shear stresses must be equal to their strength values. However, the shear failure has been studied only for widely used methods, such as the simplified Bishop method, Janbu method, Sarma method, Morgenstern method, and SRM. The tensile failure is negative.

The failure development of a slope can be prevented by an antislide tie, which can be explained by the critical state based on equations (1)~(3), and the slope control position and safety factor can be redefined as follows.

The first method: the position of slope control is chosen at the critical state for thrust- and pull-type slopes and at the yield limit stress state for the foundation pit; a rigid design is used with a safety factor, and a small deformation is permitted for this rigid design. The second method: the position of slope control is chosen at the yield limit stress state for thrust- and pull-type slopes and at the peak stress state for the foundation pit; a flexible design is applied with a safety factor, and a large deformation is allowable for this flexible design. The third method: the position of slope control is chosen between the first and the second positions, and this design can be called a "rigid-flexible" design. The force and moment balance in equations (1)~(4) must be satisfied at the design position with a safety factor, the antisliding force is the vector sum of the unbalanced thrust from the postfailure zone, and the displacement of the slope control can be calculated.

6. Shear Stress-Strain Model

The complete process shear-strain model (CPSM) must necessarily be employed to describe the progressive failure process of a slope. A stress-strain equation with four parameters is a part of the CPSM. The equation can be described by taking a shear stress and strain as an example in the following form:

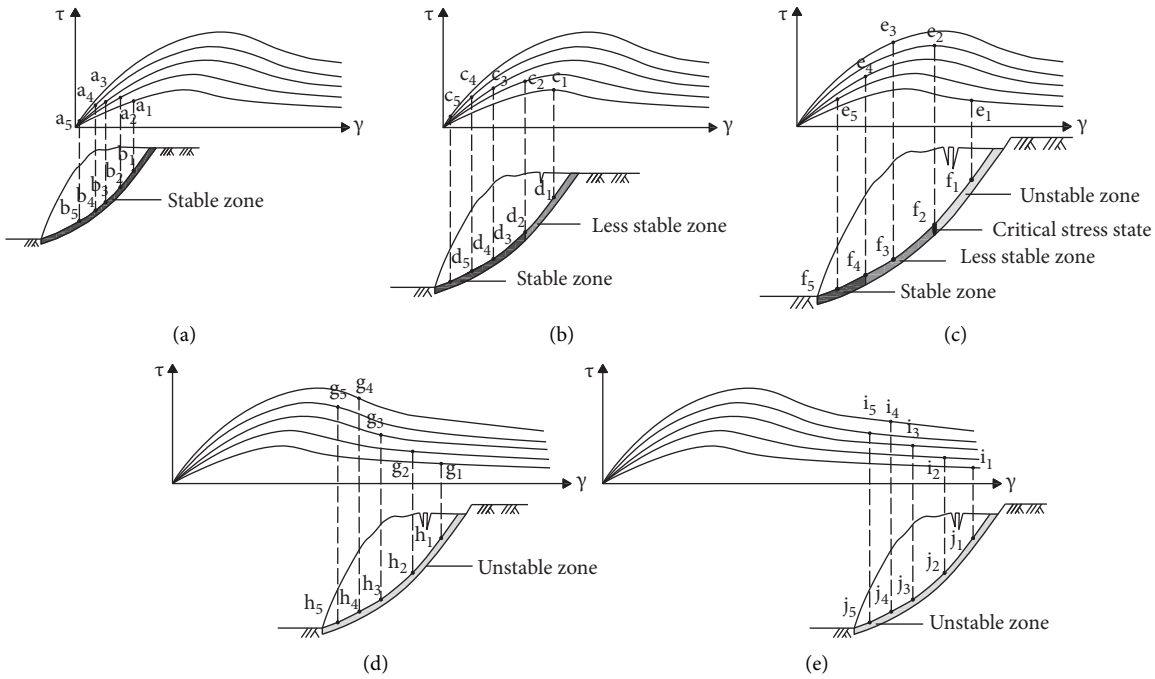

Figure 7: Five forms of the slope existing in the field.

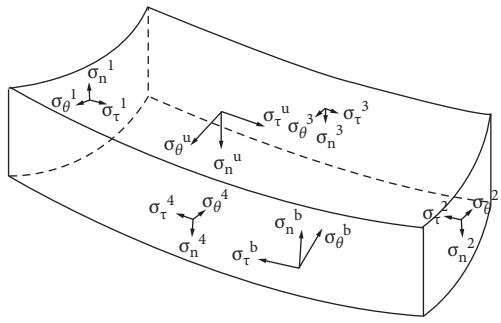

Figure 8: Schematic of a sliding surface element.

$$\tau = G\gamma\left(\frac{1+\gamma^q}{p}\right)^{\xi}, \tag{5}$$

where τ and γ are the shear stress and shear strain, respectively; G is the shear modulus dependent on the normal stress; and p, q, and ξ are the constant coefficients dependent on the normal stress. The units of τ and G are kPa.

The following conditions are needed for the rock or soil with softening mechanical behaviours:

$$\begin{aligned} 1 + q\xi &\neq 0, \\ -1 < \xi &\leq 0. \end{aligned} \tag{6}$$

The critical shear strain (defined as the shear strain corresponding to the peak shear stress) is satisfied in the following form:

$$p + (1 + q\xi)\gamma_{\text{peak}}^{q} = 0, \tag{7}$$

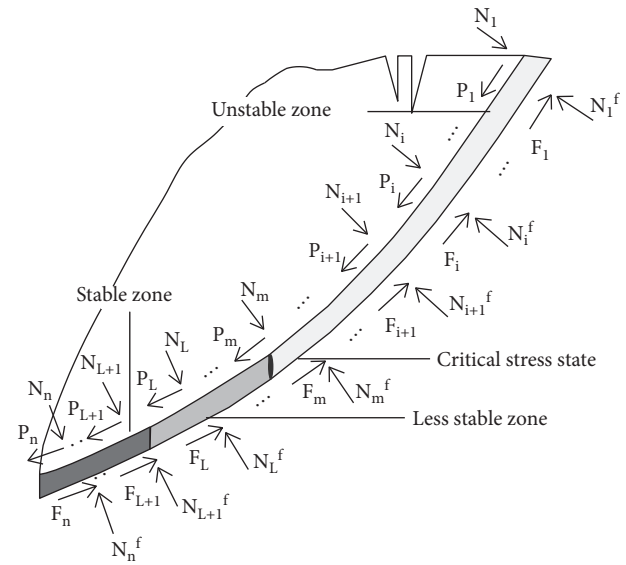

Figure 9: Distribution characteristics of force along the sliding surface of a 2D thrust-type slope.

where γ_{peak} is the critical shear strain corresponding to the critical shear stress.

The Mohr–Coulomb criterion is assumed to describe the critical shear stress (τ_{peak}) (note: other criteria can also describe the critical shear stress):

$$\tau_{\text{peak}} = C + \sigma_n \tan\varphi, \tag{8}$$

where C is the cohesion, σ_n is the normal stress, and φ is the frictional angle. The units of σ_n and C are kPa.

The critical shear strain is assumed to be related only to normal stress, and the critical shear strain (γ_{peak}) can be described as follows:

$$\left(\frac{\gamma_{\text{peak}}}{a_3}\right)^2 + \left(\frac{(\sigma_n - a_2)}{a_1}\right)^{\zeta_N} = 1, \tag{9}$$

where a_1, a_2, a_3, and ζ_N are the constant coefficients which are dependent on the normal stress; the units of a_1 and a_2 are kPa, and a_3 and ζ_N are the constant coefficients without units.

Finally,

$$G = G_0 + b_1\sigma_n + b_2\sigma_n^2, \tag{10}$$

where G_0 is the initial shear modulus when the normal stress (σ_n) is equal to zero, b_1 is a constant coefficient without units, and $b_2 = -b_1/(2a_2)$.

The softening coefficient (ξ) can be presented in the following form:

$$\xi = \frac{\xi_0}{\left(1 + (\xi_0/\xi_c - 1)(\sigma_n/\sigma_n^c)^{\varsigma}\right)}, \tag{11}$$

where ξ_0 is the value of ξ when σ_n is equal to zero, ξ_c is the value of ξ when σ_n is equal to $\sigma_n{}^c$, and ς is a constant coefficient without units. The softening coefficient can be obtained by the shear stress and shear strain complete process tests with different normal stresses.

Regarding the physical significance, it is not necessary to explain the parameters related to the Mohr–Coulomb criterion: a_2 is the critical normal stress ($a_2 = \sigma_n^{\text{crit}}$), a_3 is the critical shear strain ($a_3 = \gamma_{\text{peak}}^{\text{crit}}$) when the normal stress is equal to the critical normal stress ($a_2 = \sigma_n^{\text{crit}}$), a_1 is relative to the critical shear strain ($\gamma_{\text{peak}}^0 = a_3\sqrt{1 - (a_2/a_1)^2}$) when the normal stress is equal to zero, $a_1 > a_2\xi$ represents the softening degree of rock or soil under different normal stresses, and p and q are the representative parameters between the critical shear stress and shear strain.

7. Stability Analysis

In stability analysis, the mechanical behaviours of weak intercalated strata are key factors for the sliding body and different safety factors are proposed to describe the slope stability.

7.1. Stability Analysis of an Ideal Elastoplastic Model

7.1.1. Comprehensive Sliding-Resistance Method (CSRM). The stress fields of the landslide body along the slip surface (see Figure 10, dashed line *ABDEC* represents the sliding surface) can be obtained by the current calculation method, and the vector sums of sliding force can be obtained in the directions of *X*-, *Y*-, and *Z*-axes (see Figure 10):

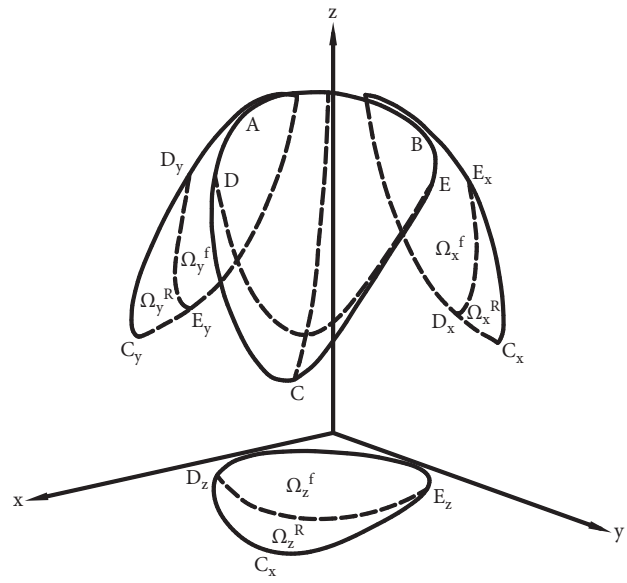

Figure 10: Distribution of failure zones and projections along the *X*-, *Y*-, and *Z*-axes.

$$\begin{aligned} P_{xs} &= \iint_{\Omega_x^f + \Omega_x^R} (\sigma_\theta^u + \sigma_\tau^u)\mathrm{d}y\mathrm{d}z, \\ P_{ys} &= \iint_{\Omega_y^f + \Omega_y^R} (\sigma_\theta^u + \sigma_\tau^u)\mathrm{d}x\mathrm{d}z, \\ P_{zs} &= \iint_{\Omega_z^f + \Omega_z^R} (\sigma_\theta^u + \sigma_\tau^u)\mathrm{d}x\mathrm{d}y, \end{aligned} \tag{12}$$

where P_{xs}, P_{ys}, and P_{zs} are the vector sums of the sliding forces in the directions of the *X*-, *Y*-, and *Z*-axes, Ω is the area of the whole integration, Ω^f is the destroyed region, and Ω^R is the nondestroyed region.

The vector sum (P_s) of P_{xs}, P_{ys}, and P_{zs} is

$$P_s = \sqrt{(P_{xs})^2 + (P_{ys})^2 + (P_{zs})^2}. \tag{13}$$

The direction cosines of P_s with Cartesian coordinate axes are α_s, β_s, and γ_s. The failure mode can be analyzed, the distribution of skid-resistance stresses ($\sigma_n^{p,b}, \sigma_\theta^{p,b}$, and $\sigma_\tau^{p,b}$) under the possible failure mode can be obtained, and the vector sums of the antislip force under the possible failure modes can be calculated in the directions of *X*-, *Y*-, and *Z*-axes:

$$\begin{aligned} T^{xT} &= \iint_{\Omega_x^f + \Omega_x^R} \left(\sigma_n^{p,b} + \sigma_\theta^{p,b} + \sigma_z^{p,b}\right)\mathrm{d}y\mathrm{d}z, \\ T^{yT} &= \iint_{\Omega_y^f + \Omega_y^R} \left(\sigma_n^{p,b} + \sigma_\theta^{p,b} + \sigma_z^{p,b}\right)\mathrm{d}x\mathrm{d}z, \\ T^{zT} &= \iint_{\Omega_y^f + \Omega_y^R} \left(\sigma_n^{p,b} + \sigma_\theta^{p,b} + \sigma_z^{p,b}\right)\mathrm{d}x\mathrm{d}y, \end{aligned} \tag{14}$$

where T^{xT}, T^{yT}, and T^{zT} are the vector sums of the stabilizing forces in the directions of the *X*-, *Y*-, and *Z*-axes under the possible failure modes.

The vector sum (T^T) of T^{xT}, T^{yT}, and T^{zT} is

$$T^T = \sqrt{\left(T^{xT}\right)^2 + \left(T^{yT}\right)^2 + \left(T^{zT}\right)^2}. \tag{15}$$

The direction cosines of T^T with Cartesian coordinate axes are α_T, β_T, and γ_T.

The vector angle (φ_c) between P_s and T^T can be described in the following form (see Figure 11):

$$\varphi_c = \arccos\left(\alpha_s\alpha_T + \beta_s\beta_T + \gamma_s\gamma_T\right). \tag{16}$$

The stable coefficient in the X-axis direction is

$$F^x_{\mathrm{CSRM}} = \frac{T^{xT}}{P_{xs}}. \tag{17}$$

The stable coefficient in the Y-axis direction is

$$F^y_{\mathrm{CSRM}} = \frac{T^{yT}}{P_{ys}}. \tag{18}$$

The stable coefficient in the Z-axis direction is

$$F^z_{\mathrm{CSRM}} = \frac{T^{zT}}{P_{zs}}. \tag{19}$$

The stable coefficient in the sliding force direction is defined as

$$F^s_{\mathrm{CRSM}} = \frac{T^T \cos\phi_c}{P_s}. \tag{20}$$

7.1.2. Main Thrust Method (MTM). The main thrust method is used only to evaluate the stability of a thrust-type landslide. The critical state curves (see Figure 10, dashed line DE) can be obtained, and the residual thrust force from the posterior region to the critical state curve (DE) can be calculated (see Figure 10):

$$\begin{aligned} P_{xp} &= \iint_{\Omega^f_x}\left(\sigma^u_\theta + \sigma^u_\tau - \sigma^b_\theta - \sigma^b_\tau\right)\mathrm{d}y\mathrm{d}z, \\ P_{yp} &= \iint_{\Omega^f_x}\left(\sigma^u_\theta + \sigma^u_\tau - \sigma^b_\theta - \sigma^b_\tau\right)\mathrm{d}x\mathrm{d}z, \\ P_{zp} &= \iint_{\Omega^f_x}\left(\sigma^u_\theta + \sigma^u_\tau - \sigma^b_\theta - \sigma^b_\tau\right)\mathrm{d}x\mathrm{d}y. \end{aligned} \tag{21}$$

The vector sum (P^p) of P_{xp}, P_{yp}, and P_{zp} is

$$P^p = \sqrt{\left(P_{xp}\right)^2 + \left(P_{yp}\right)^2 + \left(P_{zp}\right)^2}. \tag{22}$$

The direction cosines of P^p with Cartesian coordinate axes are α_p, β_p, and γ_p.

The differential value (or residual frictional force) between the frictional force $(\sigma^{p,b}_n, \sigma^{p,b}_\theta$, and $\sigma^{p,b}_\tau)$ under the possible failure mode and the antislip force $(\sigma^b_n, \sigma^b_\theta$, and $\sigma^b_\tau)$ under the current situation can be obtained as follows:

$$\begin{aligned} T^{xp} &= \iint_{\Omega^R_x}\left(\sigma^{p,b}_n + \sigma^{p,b}_\theta + \sigma^{p,b}_\tau - \sigma^b_n - \sigma^b_\theta - \sigma^b_\tau\right)\mathrm{d}y\mathrm{d}z, \\ T^{yp} &= \iint_{\Omega^R_y}\left(\sigma^{p,b}_n + \sigma^{p,b}_\theta + \sigma^{p,b}_\tau - \sigma^b_n - \sigma^b_\theta - \sigma^b_\tau\right)\mathrm{d}x\mathrm{d}z, \\ T^{zp} &= \iint_{\Omega^R_z}\left(\sigma^{p,b}_n + \sigma^{p,b}_\theta + \sigma^{p,b}_\tau - \sigma^b_n - \sigma^b_\theta - \sigma^b_\tau\right)\mathrm{d}y\mathrm{d}x. \end{aligned} \tag{23}$$

The vector sum (T^p) of $F_p{}^x, F_p{}^y$, and $F_p{}^z$ is

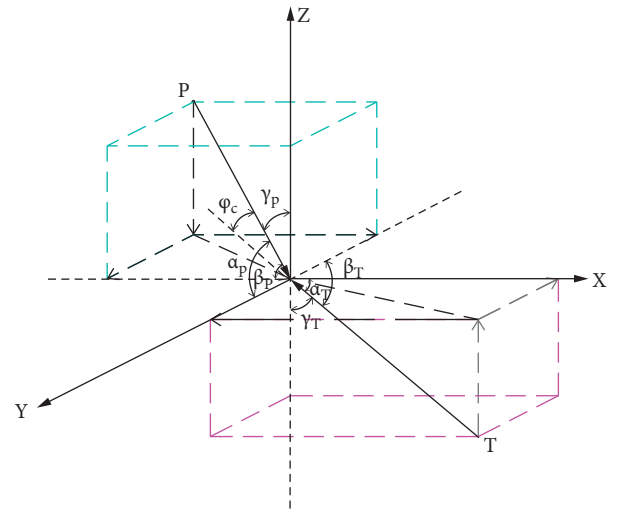

Figure 11: Vector and relation diagram of glide force and antislip force in potentially destructive mode.

$$T^p = \sqrt{\left(T_{xp}\right)^2 + \left(T_{yp}\right)^2 + \left(T_{zp}\right)^2}. \tag{24}$$

The direction cosines of T^p with Cartesian coordinate axes are α_r, β_r, and γ_r.

The vector angle (φ_m) between P^p and $F_{sf} = \mathrm{TSF} - F_{lf}$ can be described in the following form:

$$\alpha_m = \arccos\left(\alpha_p\alpha_r + \beta_p\beta_r + \gamma_p\gamma_r\right). \tag{25}$$

The stable coefficient in the X-axis direction is

$$F^x_{\mathrm{MTM}} = \frac{T^{xp}}{P_{xp}}. \tag{26}$$

The stable coefficient in the Y-axis direction is

$$F^y_{\mathrm{MTM}} = \frac{T^{yp}}{P_{yp}}. \tag{27}$$

The stable coefficient in the Z-axis direction is

$$F^z_{\mathrm{MTM}} = \frac{T^{zp}}{P_{zp}}. \tag{28}$$

The stable coefficient in the main slip force direction is

$$F^s_{\mathrm{MTM}} = \frac{T^p \cos\phi_m}{P^p}. \tag{29}$$

7.1.3. Comprehensive Displacement Method (CDM). The deformation from the present strain states $(\varepsilon^u_\theta$ and $\varepsilon^u_\tau)$ is calculated and is projected onto X-, Y-, and Z-axes:

$$\begin{aligned} S_{xd} &= \iint_{\Omega^f_x+\Omega^R_x}\left(\varepsilon^u_\theta + \varepsilon^u_\tau\right)\mathrm{d}y\mathrm{d}z, \\ S_{yd} &= \iint_{\Omega^f_y+\Omega^R_y}\left(\varepsilon^u_\theta + \varepsilon^u_\tau\right)\mathrm{d}x\mathrm{d}z, \\ S_{zd} &= \iint_{\Omega^f_z+\Omega^R_z}\left(\varepsilon^u_\theta + \varepsilon^u_\tau\right)\mathrm{d}x\mathrm{d}y. \end{aligned} \tag{30}$$

The vector sum (α_i) of c_i is

$$S_d = \sqrt{(S_{x\,d})^2 + (S_{y\,d})^2 + (S_{z\,d})^2}. \tag{31}$$

The direction cosines of F with Cartesian coordinate axes are σ_n^i. The possible failure mode is analyzed, the distribution of the strain ($\varepsilon_n^{p,b}$, $\varepsilon_\theta^{p,b}$, and $\varepsilon_\tau^{p,b}$) under the possible failure mode can be calculated, and the vector sums of displacement under the possible failure mode can be obtained in the directions of X-, Y-, and Z-axes:

$$\begin{aligned} S^{xd} &= \iint_{\Omega_x^f + \Omega_x^R} \left(\varepsilon_n^{p,b} + \varepsilon_\theta^{p,b} + \varepsilon_\tau^{p,b}\right) \mathrm{d}y\mathrm{d}z. \\ S^{yd} &= \iint_{\Omega_y^f + \Omega_y^R} \left(\varepsilon_n^{p,b} + \varepsilon_\theta^{p,b} + \varepsilon_\tau^{p,b}\right) \mathrm{d}x\mathrm{d}z, \\ S^{zd} &= \iint_{\Omega_z^f + \Omega_z^R} \left(\varepsilon_n^{p,b} + \varepsilon_\theta^{p,b} + \varepsilon_\tau^{p,b}\right) \mathrm{d}y\mathrm{d}x. \end{aligned} \tag{32}$$

The vector sum (S^d) of $S^{x\,d}, S^{y\,d}$, and $S^{z\,d}$ is

$$S^d = \sqrt{\left(S^{x\,d}\right)^2 + \left(S^{y\,d}\right)^2 + \left(S^{z\,d}\right)^2}. \tag{33}$$

The direction cosines of S^d with Cartesian coordinate axes are α^d, β^d, and γ^d. The vector angle (φ_d) between the vectors S^d and S_d can be calculated as follows:

$$\varphi_d = \arccos\left(\alpha^d \alpha_d + \beta^d \beta_d + \gamma^d \gamma_d\right). \tag{34}$$

The stable coefficient in the X-axis direction is

$$F_{C\,DM}^x = \frac{S^{xd}}{S_{xd}}. \tag{35}$$

The stable coefficient in the Y-axis direction is

$$F_{C\,DM}^y = \frac{S^{yd}}{S_{yd}}. \tag{36}$$

The stable coefficient in the Z-axis direction is

$$F_{\mathrm{CDM}}^z = \frac{S^{zd}}{S_{zd}}. \tag{37}$$

The stable coefficient in the slip displacement direction is

$$F_{C\,DM}^s = S^d \cos\,\phi_d / S^d. \tag{38}$$

7.1.4. Surplus Displacement Method (SDM). The strains (ε_θ^u and ε_τ^u) from the posterior region to the critical stress state (see Figure 10, DE (dashed line)) in the present status are calculated and are projected onto X-, Y-, and Z-axes:

$$\begin{aligned} S_{xs} &= \iint_{\Omega_x^f} \left(\varepsilon_\theta^u + \varepsilon_\tau^u\right) \mathrm{d}y\mathrm{d}z, \\ S_{ys} &= \iint_{\Omega_y^f} \left(\varepsilon_\theta^u + \varepsilon_\tau^u\right) \mathrm{d}x\mathrm{d}z, \\ S_{zs} &= \iint_{\Omega_z^f} \left(\varepsilon_\theta^u + \varepsilon_\tau^u\right) \mathrm{d}x\mathrm{d}y, \end{aligned} \tag{39}$$

where S_{xs}, S_{ys}, and S_{zs} are the vector sums of the displacements in the directions of the X-, Y-, and Z-axes, respectively, and the vector sum (S_s) of S_{xs}, S_{ys}, and S_{zs} is

$$S_s = \sqrt{\left(S_{xs}\right)^2 + \left(S_{ys}\right)^2 + \left(S_{zs}\right)^2}. \tag{40}$$

The direction cosines of S_s with Cartesian coordinate axes are α_s, β_s, and γ_s. The possible failure mode is analyzed, and the distribution of the strain ($\varepsilon_n^{p.b}$, $\varepsilon_\theta^{p.b}$, and $\varepsilon_\tau^{p.b}$) under the possible failure mode can be calculated. The differences between $\varepsilon_n^{p.b}$, $\varepsilon_\theta^{p.b}$, and $\varepsilon_\tau^{p.b}$ and $\varepsilon_n^b, \varepsilon_\theta^b$, and ε_τ^b can be obtained and projected in the directions of the X-, Y-, and Z-axes:

$$\begin{aligned} S^{xs} &= \iint_{\Omega_x^k} \left(\varepsilon_n^{p,b} + \varepsilon_\theta^{p,b} + \varepsilon_\tau^{p,b} - \varepsilon_n^b - \varepsilon_\theta^b - \varepsilon_\tau^b\right) \mathrm{d}y\mathrm{d}z, \\ S^{ys} &= \iint_{\Omega_y^k} \left(\varepsilon_n^{p,b} + \varepsilon_\theta^{p,b} + \varepsilon_\tau^{p,b} - \varepsilon_n^b - \varepsilon_\theta^b - \varepsilon_\tau^b\right) \mathrm{d}x\mathrm{d}z, \\ S^{zs} &= \iint_{\Omega_z^k} \left(\varepsilon_n^{p,b} + \varepsilon_\theta^{p,b} + \varepsilon_\tau^{p,b} - \varepsilon_n^b - \varepsilon_\theta^b - \varepsilon_\tau^b\right) \mathrm{d}y\mathrm{d}x, \end{aligned} \tag{41}$$

where S^{xs}, S^{ys}, and S^{zs} are the vector sums of the displacement differences in the directions of the X-, Y-, and Z-axes between the possible failure mode and present status, respectively. The vector sum (S^s) of S^{xs}, S^{ys}, and S^{zs} is

$$S^s = \sqrt{\left(S^{xs}\right)^2 + \left(S^{ys}\right)^2 + \left(S^{zs}\right)^2}. \tag{42}$$

The direction cosines of S^s with Cartesian coordinate axes are α^s, β^s, and γ^s. The vector angle (φ_s) between the vectors S^s and S_s can be calculated:

$$\varphi_s = \arccos\left(\alpha^s \alpha_s + \beta^s \beta_s + \gamma^s \gamma_s\right). \tag{43}$$

The stable coefficient in the X-axis direction is

$$F_{S\,DM}^x = \frac{S^{xs}}{S_s}. \tag{44}$$

The stable coefficient in the Y-axis direction is

$$F_{S\,DM}^y = \frac{S^{ys}}{S_s}. \tag{45}$$

The stable coefficient in the Z-axis direction is

$$F_{S\,DM}^z = \frac{S^{zs}}{S_s}. \tag{46}$$

The stable coefficient in the main slip displacement direction is

$$F_{S\,DM}^s = \frac{S^s \cos\,\phi_s}{S_s}. \tag{47}$$

7.2. Stability Analysis of a New Shear Stress Constitutive Model. According to the stability analysis method of the ideal elastoplastic constitutive model in Section 7.1, the stability coefficient of the new shear stress constitutive models, such as the *CSRM*, the *MTM*, and the surplus displacement method (*SDM*), can be obtained.

7.3. Stability Coefficient Study

7.3.1. Some Term Definitions. Some terms are first defined. The failure ratio (f_r) is the value of the driving stress of rock or soil divided by its strength; when the value is greater than 1, the f_r is equal to 1. The failure percentage (f_p) is the value of the sum of the failure ratio multiplied by its area and divided by the total area. The failure area percentage (f_s) is the value of the area sum corresponding to the failure ratio ($f_r = 1$) divided by the total area.

The frictional resistance variation coefficient (F_f) is the vector sum of the frictional resistance of the entire sliding body failure divided by the frictional resistance vector sum during the progressive deformation and includes the X-, Y-, and Z-axial (F_f^x, F_f^y, and F_y^z) and vector sum (F_f) directions. The variation coefficient of the driving sliding force (F_p) is the vector sum of the driving sliding force of the entire sliding surface failure divided by the driving sliding force vector sum during the progressive deformation and includes the X-, Y-, and Z-axial (F_p^x, F_p^y, and F_p^z) and vector sum (F_p) directions.

7.3.2. Comparison of Safety Factors. A partial strength reduction method is proposed, and its result is used to compare with the progressive failure analysis. The steps of the partial strength reduction method are as follows.

First, the traditional safety factor (TSF) of the entire sliding body is calculated by the traditional slice block method. Then, the local safety factor (F_{lf}) from the rear zone to the critical state (Figure 12, where the m-th slice block is assumed to be in a critical stress state under $F_{lf} = 1$) is obtained by the same method. The surplus safety factor ($F_{sf} = \text{TSF} - F_{lf}$) is equal to the safety factor of the entire sliding body minus the local safety factor. This factor is used to compare with that of the MTM during the progressive failure process.

7.3.3. Unbalanced Thrust Method. The unbalanced thrust method (UTM) is taken as an example to calculate the safety factor, and its formula is derived (Figure 13).

The fundamental assumptions are as follows:

(1) The slice block is assumed to have strong deformation capacity and is classified by a vertical interval

(2) The former slice block force from the posterior slice block is parallel to the bottom side of the posterior slice block

(3) The rotation of the slice block is not considered

(4) The frictional stress is satisfied with the new shear stress-strain model

The relationship between the shear strain of two slice blocks can be described in the failure zone as follows:

$$\gamma_i = \frac{\gamma_{i+1}}{\cos\left(\alpha_i - \alpha_{i+1}\right)}. \tag{48}$$

In the i-th slice block, we have the following.

Normal pressure N_i is

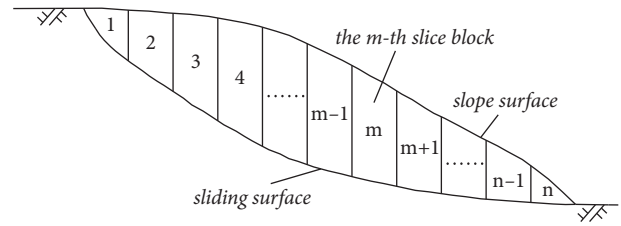

Figure 12: Schematic of the partial strength reduction method.

$$N_i = W_i \cos\alpha_i + P_{i-1}\sin\left(\alpha_{i-1} - \alpha_i\right) + \frac{1}{2}\gamma_w h_{i,u}^2 \sin\alpha_i - \frac{1}{2}\gamma h_{i,b}^2 \sin\alpha_i - \frac{1}{2}\left(\gamma_i h_{i,u} + \gamma_i h_{i,b}\right) l_i. \tag{49}$$

Normal stress σ_n^i is

$$\sigma_n^i = \frac{N_i}{l_i}. \tag{50}$$

Critical frictional stress τ_{peak}^i is

$$\tau_{\text{peak}}^i = c_i + \sigma_n^i \tan\varphi_i. \tag{51}$$

Critical frictional resistance T_{peak}^i is

$$T_{\text{peak}}^i = c_i l_i + N_i \tan\varphi_i. \tag{52}$$

Frictional force after strength reduction $T_{\text{peak},F}^i$ is

$$T_{\text{peak},F}^i = \frac{T_{\text{peak}}^i}{F}. \tag{53}$$

Driving sliding force P_i^S ($P_0 = 0$) is

$$P_i^S = W_i \sin\alpha_i + P_{i-1}\cos\left(\alpha_{i-1} - \alpha_i\right) + \frac{1}{2}\gamma_w h_{i,u}^2 \cos\alpha_i - \frac{1}{2}\gamma_w h_{i,b}^2 \cos\alpha_i. \tag{54}$$

Unbalanced thrust force P_i is

$$P_i = P_i^S - T_{\text{peak},F}^i, \tag{55}$$

where W_i is the weight of the i-th slice block, l_i is the length of the i-th slice block bottom, α_i is the angle between the bottom and the horizontal axis of the i-th slice block, c_i is the cohesion of the bottom of the i-th slice block, φ_i is the frictional angle of the i-th slice block, F is the stability factor, σ_n^i is the normal stress of the i-th slice block, γ_w is the specific gravity of water, $h_{i,u}$ is the height of water at the left of the slice block, and $h_{i,b}$ is the height of water level at the right of the slice block.

8. Case Study

The progressive failure process is presented for the Kaziwan landslide in the Three Gorges Reservoir.

8.1. Geological Survey. The Kaziwan landslide is situated in Zigui County, and its geographic coordinates are as follows:

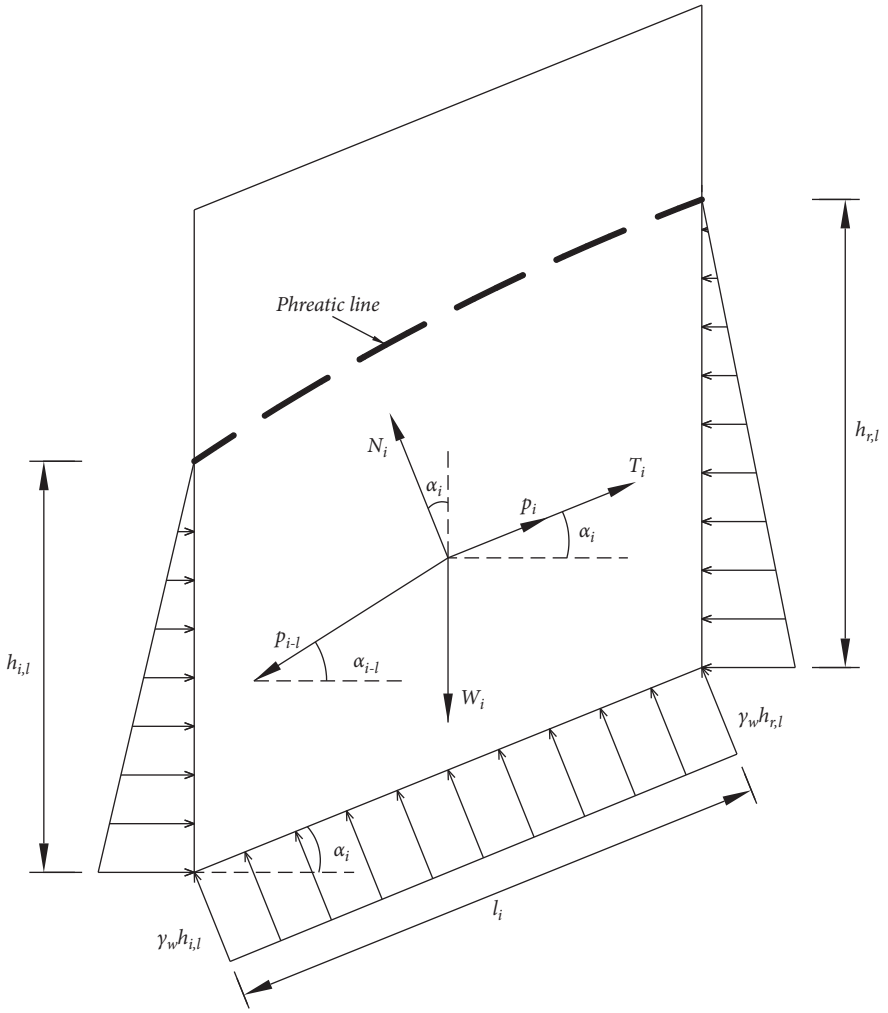

Figure 13: The force distribution of the i-th soil slice block.

(X: 3432550, Y: 37471500), longitude: 110°41′37″E, and latitude: 31° 0′48″N. The Kaziwan landslide is located on the left bank of the Guizou River, 1.9 km from the mouth and 44 km from the Three Gorges Dam. Its basic characteristics are as follows. The trailing edge elevation is 720 m, the leading edge elevation is 85 m, the slope aspect is 296°, the slope length is 1270 m, the slope height is 635 m, and the slope degree is 15°~40° (Figure 14).

Quaternary deposits are distributed across the slope. The deposits consist of broken stone and silty clay. Most stone is located at the toe of the slope; boulders can be seen in the front, the particle sizes range from 0.4 m to 1.0 m, and the largest is more than 1.0 m. The stratigraphic lithology is interbedded sandstone and mudstone of the Upper Jurassic Suining Formation. The purple-red silty mudstone, siltstone, and feldspar sandstone crop out the northeast of the slope. The occurrence of bedrock is 280°~320°∠26°~39°, and the occurrences of fissures are 180°∠82° and 240~250°∠46~79°. Cracks are filled with mudstone. The lateral bedrock crops out to the southwest, and its occurrence is 65°∠66°. The Kaziwan slope is downward.

The Guizhou River is an open face of the Kaziwan landslide. Its left boundary direction is 340°, and its length is 1000 m; the terrain gradient at the boundary is gentle, and the gradient is approximately 20°. Its right boundary direction is 210°, and its length is 1000 m. The landslide is composed of sandstone and mudstone, which are easily softened by water immersion to form a weak layer. The sliding zone between the sandstone and mudstone is formed naturally.

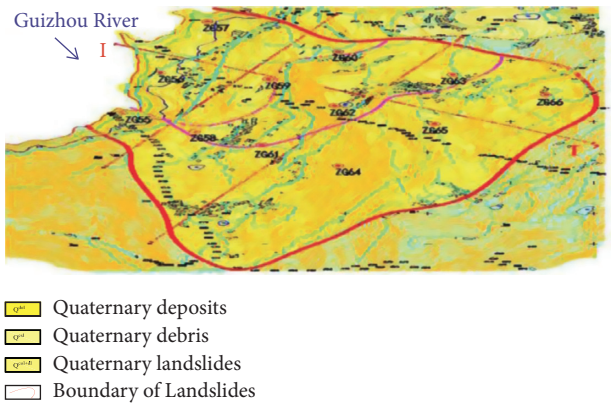

Figure 14: Plan view of the Kaziwan landslide.

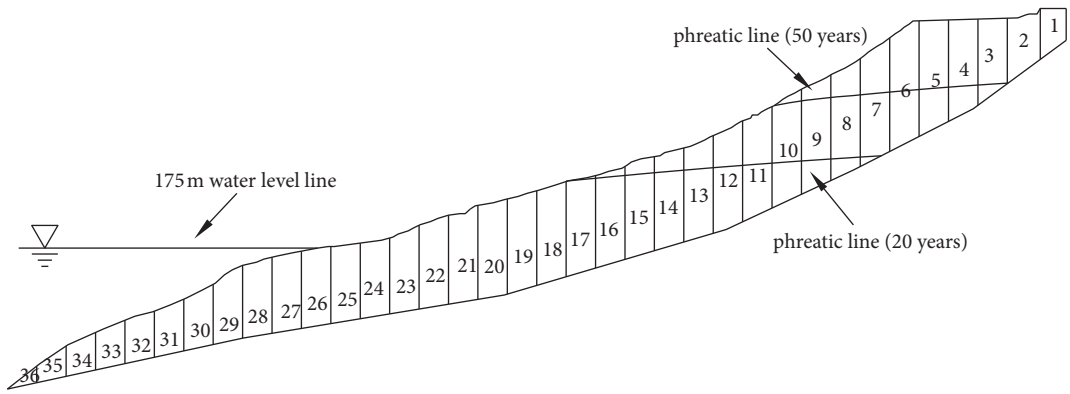

Figure 15: Block division map of the Kaziwan landslide.

Table 1: Safety factor of progressive failure under the rainfall with a recurrence interval of 20 years.

CSB	25	26	27	28	29	30
TSF	1.317	1.349	1.399	1.410	1.428	1.484
F^x_{CSRM}	0.746	0.704	0.655	0.607	0.559	0.510
F^y_{CSRM}	2.925	2.808	2.667	2.526	2.385	2.244
F^s_{CSRM}	1.718	1.558	1.540	1.523	1.475	1.410
F^x_{MTM}	0.202	0.193	0.175	0.157	0.124	0.108
F^y_{MTM}	0.205	0.197	0.186	0.172	0.147	0.121
F^s_{MTM}	0.203	0.195	0.189	0.166	0.135	0.111
F^x_{CDM}	1.152	1.141	1.133	1.117	1.102	1.088
F^y_{CDM}	1.238	1.206	1.193	1.181	1.172	1.162
F^s_{CDM}	1.188	1.175	1.161	1.157	1.144	1.133
F^x_{SDM}	0.284	0.268	0.256	0.211	0.185	0.163
F^y_{SDM}	0.402	0.392	0.342	0.319	0.288	0.267
F^s_{SDM}	0.344	0.333	0.326	0.300	0.282	0.236
CSB	31	32	33	34	35	36
TSF	1.495	1.508	1.519	1.544	1.559	1.587
F^x_{CSRM}	0.462	0.414	0.365	0.317	0.269	0.220
F^y_{CSRM}	2.103	1.962	1.821	1.680	1.539	1.398
F^s_{CSRM}	1.320	1.290	1.214	1.117	1.049	1.011
F^x_{MTM}	0.097	0.075	0.043	0.024	0.018	0.00
F^y_{MTM}	0.101	0.092	0.067	0.043	0.037	0.00
F^s_{MTM}	0.099	0.084	0.046	0.029	0.021	0.00
F^x_{CDM}	1.064	1.053	1.042	1.035	1.025	1.00
F^y_{CDM}	1.142	1.121	1.101	1.090	1.070	1.00
F^s_{CDM}	1.120	1.110	1.075	1.055	1.020	1.00
F^x_{SDM}	0.142	0.109	0.081	0.048	0.026	0.00
F^y_{SDM}	0.253	0.218	0.173	0.127	0.071	0.00
F^s_{SDM}	0.215	0.193	0.122	0.101	0.054	0.00

The normal deformation is neglected.

8.2. Calculation and Analysis. The calculated slice block scheme (Figure 15) can be obtained along the profile I-I' (Figure 14). The specific weight of the sliding body is 20 kN/m^3, and the angle and length of the bottom margin of the slice block can be seen in Figure 15.

The parameters of the model are listed as follows:

$$c = 24\,\mathrm{kPa},$$

$$\phi = 23^{\circ},$$

$$G = 2850\,\mathrm{kPa},$$

$$\begin{aligned}
\rho_{i,0} &= -0.9999,\\
\rho_{i,c} &= -0.51,\\
\sigma_i^{n,c} &= 900\,\mathrm{kPa},\\
\varsigma_i &= 1.28,\\
a_{i,3} &= 0.0129,\\
a_{i,2} &= 1500\,\mathrm{kPa},\\
a_{i,1} &= 2000\,\mathrm{kPa},\\
b_1 &= 50,\\
b_2 &= 0\left(\frac{1}{\mathrm{kPa}}\right).
\end{aligned} \tag{56}$$

The rainfall with a recurrence interval of 20 years is researched, and the seepage curve can be obtained by numerical analysis. The TSF is 1.587.

The critical stress state is located in the 25th slice block, when the partial strength reduction method proposed in this paper is used and the safety factor is equal to 1. When the critical state block (CSB) moves forward step by step, the different safety factors are presented (Table 1) under the rainfall with a recurrence interval of 20 years.

The rainfall once in 50 years is also researched, and the TSF is 1.462. The critical stress state is located at the 30th slice block, when the partial strength reduction method proposed in this paper is used and the safety factor is equal to 1. When the CSB moves forward step by step, the different safety factors are presented (see Table 2) under the rainfall once in 50 years.

The TSFs (1.587 and 1.462) are obtained under the rainfall once in 20 and 50 years, respectively. The surplus safety factors are 0.587 and 0.462, respectively, but the safety factors obtained by the MTM are 0.202, 0.203, 0.203 and 0.097, 0.101, 0.099 in the X-axial, Y-axial, and main sliding directions, respectively. These results show that the surplus safety factors (0.587, 0.462) obtained by the traditional method are greater than those (0.203, 0.099) of the new method (MTM) proposed in this paper.

Tables 1 and 2 show that the safety factor decreases while the critical stress state moves forward step by step. Finally, when the 36th slice block is in the critical stress state, the safety factors of MTM and SDM are equal to 0 and the safety

Table 2: Safety factor of progressive failure under once in 50 years of heavy rain.

CSB	30	31	32	33	34	35	36
TSF	1.21	1.344	1.407	1.415	1.433	1.447	1.462
F^x_{CSRM}	0.595	0.527	0.469	0.394	0.340	0.264	0.210
F^y_{CSRM}	2.645	2.454	2.246	2.073	1.845	1.665	1.456
F^s_{CSRM}	1.743	1.643	1.439	1.350	1.156	1.076	0.976
F^x_{MTM}	0.100	0.071	0.048	0.035	0.028	0.017	0.00
F^y_{MTM}	0.197	0.131	0.107	0.086	0.054	0.031	0.00
F^s_{MTM}	0.120	0.085	0.068	0.052	0.034	0.019	0.00
F^x_{CDM}	1.210	1.193	1.114	1.094	1.055	1.024	1.00
F^y_{CDM}	1.310	1.258	1.200	1.177	1.126	1.069	1.00
F^s_{CDM}	1.227	1.199	1.120	1.108	1.069	1.019	1.00
F^x_{SDM}	0.140	0.107	0.079	0.067	0.041	0.033	0.00
F^y_{SDM}	0.271	0.217	0.171	0.128	0.077	0.039	0.00
F^s_{SDM}	0.191	0.161	0.129	0.080	0.055	0.036	0.00

The normal deformation is neglected.

factor of CDM is equal to 1; thus, the entire Kaziwan landslide maintains the critical state. The physical significance of the MTM, SDM, and CDM are very clear.

9. Conclusion

The failure rule for a slope is investigated, and several results are obtained in this paper. The failure development direction is defined, and the mechanical failure mode can be deduced from the cracking trajectories of the slope.

Five failure modes are proposed for thrust-type slopes. In mode I, shear failure occurs. In mode II, tensile (or tensile-shear) failure occurs in the rear zone and shear failure occurs in the other zones. In mode III, tensile (or tensile-shear) failure occurs in the front zone and shear failure occurs in the other zones. In mode IV, the mechanical failure mode is a combination of modes II and III. In mode V, mechanical failure occurs by alternating shear-tensile-shear modes. That the failure occurs is defined along the sliding surface.

For pull-type slopes, in mode I, shear failure occurs along the whole sliding surface. In mode II, shear failure occurs in the front zone and tensile (or tensile-shear) failure occurs in the rear zone. In mode III, shear failure occurs in the front zone and tensile failure occurs in the rear zone of the sliding body. Mode IV corresponds to a rock mass with distributed joints (or fissures): shear, tensile, and shear failures occur alternately along the soft interlayer and joints (or fissures). Mode V is a combination of mode IV and a shear failure (or tensile-shear or tensile failure).

Five existing forms in the field are proposed for slopes. In form I, the stress distribution is within the yield limit stress state. In form II, the various states of elastic, elastoplastic, and peak stresses are distributed in different zones. In form III, the states of previous peak, peak, postfailure, and residual stresses are distributed. In form IV, the postfailure and residual stress states are present. In form V, the entire sliding surface is in the residual stress state. The stress distribution is designated to follow the sliding surface.

The force distribution characteristics are analyzed along the sliding surface; the driving sliding force is greater than the frictional resistance in the postfailure zone, and the pressure is equal to the counterpressure corresponding to the critical state. The driving sliding force and pressure are equal to the frictional resistance and counterpressure, respectively, in the stable and less-stable zones and at the critical state, but the frictional resistance reaches its maximum at the critical state and both shear stress and shear strain are discontinuous in the failure zone.

The stability of the slope is directly related to the critical state. The force and moment balance corresponding to the material strength are used to describe the critical state for the slice method. Design methods for slope control are proposed according to the failure characteristics. In method I, a rigid design is suggested; the slope control position is selected at the critical state for the thrust- and pull-type slopes and at the yield limit stress state for the foundation pit with a safety factor. In method II, a flexible design is proposed; the slope control position is selected at the yield limit stress state for the thrust- and pull-type slopes and at the peak limit stress state for the foundation pit with a safety factor. In method III, a rigid-flexible design is proposed, and the slope control position is selected between those of methods I and II with a safety factor.

Some terms (failure ratio, etc.) are defined, and they are used for mechanical analysis and probability theory application to slope engineering. The definition of the TSF (the maximum frictional resistance divided by the driving sliding force) is worth discussing, and it is possible for the TSF to evaluate an element (or a slice block). The research results show that the MTM, CDM, and SDM are feasible for evaluating the stability of a slope with regressive failure.

Data Availability

The data used to support the findings of this study are included within the article.

Conflicts of Interest

The authors declare that they have no conflicts of interest.

Acknowledgments

This work was supported by the National Natural Science Foundation of China (Grant nos. 42071264 and 41372363). This work was also supported by the Sichuan Science and Technology Program (Grant no. 2019JDJQ0018) and supported by the Fundamental Research Funds for the Central Universities (Grant no. 2682018GJ02).

References

[1] G.-L. Feng, X.-T. Feng, B.-r. Chen, Y.-X. Xiao, and Y. Yu, "A microseismic method for dynamic warning of rockburst development processes in tunnels," *Rock Mechanics and Rock Engineering*, vol. 48, no. 5, pp. 2061–2076, 2015.

[2] G.-l. Feng, B.-r. Chen, Q. Jiang, Y.-x. Xiao, W.-j. Niu, and P.-x. Li, "Excavation-induced microseismicity and rockburst occurrence: similarities and differences between deep parallel tunnels with alternating soft-hard strata," *Journal of Central South University*, vol. 28, no. 2, pp. 582–594, 2021.

[3] W. Fellenius, "Calculation of stability of earth dam," in *Proceedings of the Transactions. 2nd congress large dams*, vol. 4, pp. 445–462, Washington, DC, USA, September 1936.
[4] A. W. Bishop, "The use of the slip circle in the stability analysis of slopes," *Géotechnique*, vol. 5, no. 1, pp. 7–17, 1955.
[5] E. Spencer, "A method of analysis of the stability of embankments assuming parallel inter-slice forces," *Géotechnique*, vol. 17, no. 1, pp. 11–26, 1967.
[6] N. Janbu, "Slope stability computations," *International Journal of Rock Mechanics and Mining Science & Geomechanics Abstracts*, vol. 12, no. 4, p. 67, 1975.
[7] S. K. Sarma and D. Tan, "Determination of critical slip surface in slope analysis," *Géotechnique*, vol. 56, no. 8, pp. 539–550, 2006.
[8] M. K. Kelesoglu, "The evaluation of three-dimensional effects on slope stability by the strength reduction method," *KSCE Journal of Civil Engineering*, vol. 20, no. 1, pp. 229–242, 2016.
[9] T.-K. Nian, R.-Q. Huang, S.-S. Wan, and G.-Q. Chen, "Three-dimensional strength-reduction finite element analysis of slopes: geometric effects," *Canadian Geotechnical Journal*, vol. 49, no. 5, pp. 574–588, 2012.
[10] H. N. Gharti, D. Komatitsch, V. Oye, R. Martin, and J. Tromp, "Application of an elastoplastic spectral-element method to 3D slope stability analysis," *International Journal for Numerical Methods in Engineering*, vol. 91, no. 1, pp. 1–26, 2012.
[11] R. C. Tiwari, N. P. Bhandary, and R. Yatabe, "3D SEM Approach to evaluate the stability of large-scale landslides in Nepal Himalaya," *Geotechnical & Geological Engineering*, vol. 33, no. 4, pp. 773–793, 2015.
[12] D. Y. Zhu and C. F. Lee, "Explicit limit equilibrium solution for slope stability," *International Journal for Numerical and Analytical Methods in Geomechanics*, vol. 26, no. 15, pp. 1573–1590, 2002.
[13] R. Baker, "Nonlinear Mohr envelopes based on triaxial data," *Journal of Geotechnical and Geoenvironmental Engineering*, vol. 130, no. 5, pp. 498–506, 2004.
[14] W. B. Wei, Y. M. Cheng, and L. Li, "Three-dimensional slope failure analysis by the strength reduction and limit equilibrium methods," *Computers and Geotechnics*, vol. 36, no. 1-2, pp. 70–80, 2009.
[15] C. Matthews, Z. Farook, and P. Helm, "Slope stability analysis-limit equilibrium or the finite element method," *Ground Engineering*, vol. 48, no. 5, pp. 22–28, 2014.
[16] X. P. Zhou and H. Cheng, "Stability analysis of three-dimensional seismic landslides using the rigorous limit equilibrium method," *Engineering Geology*, vol. 174, no. 8, pp. 87–102, 2014.
[17] L. Faramarzi, M. Zare, A. Azhari, and M. Tabaei, "Assessment of rock slope stability at cham-shir dam power plant pit using the limit equilibrium method and numerical modeling," *Bulletin of Engineering Geology and the Environment*, vol. 76, no. 2, pp. 783–794, 2016.
[18] G. Sun, Y. Yang, W. Jiang, and H. Zheng, "Effects of an increase in reservoir drawdown rate on bank slope stability: a case study at the Three Gorges Reservoir, China," *Engineering Geology*, vol. 221, pp. 61–69, 2017.
[19] X. P. Zhou and H. Cheng, "Analysis of stability of three-dimensional slopes using the rigorous limit equilibrium method," *Engineering Geology*, vol. 160, pp. 21–33, 2013.
[20] H. Zheng, Z. L. Yang, and G. H. Sun, "Extremum solutions to the limit equilibrium method subjected to physical admissibility," *Natural Hazards*, vol. 65, no. 1, pp. 79–96, 2013.
[21] X. Lü, D. Xue, Q. Chen, X. Zhai, and M. Huang, "Centrifuge model test and limit equilibrium analysis of the stability of municipal solid waste slopes," *Bulletin of Engineering Geology and the Environment*, vol. 78, no. 4, pp. 3011–3021, 2019.
[22] B. Nilsen, "Rock slope stability analysis according to Eurocode 7, discussion of some dilemmas with particular focus on limit equilibrium analysis," *Bulletin of Engineering Geology and the Environment*, vol. 76, no. 4, pp. 1229–1236, 2016.
[23] X. P. Zhou and H. Cheng, "The long-term stability analysis of 3D creeping slopes using the displacement-based rigorous limit equilibrium method," *Engineering Geology*, vol. 195, pp. 292–300, 2015.
[24] A. Su, Z. Zou, Z. Lu, and J. Wang, "The inclination of the interslice resultant force in the limit equilibrium slope stability analysis," *Engineering Geology*, vol. 240, no. 5, pp. 140–148, 2018.
[25] B. Thiebes, R. Bell, T. Glade, S. Jäger, M. Anderson, and L. Holcombe, "A WebGIS decision-support system for slope stability based on limit-equilibrium modelling," *Engineering Geology*, vol. 158, pp. 109–118, 2013.
[26] J. Shen, M. Karakus, and C. Xu, "Chart-based slope stability assessment using the Generalized Hoek-Brown criterion," *International Journal of Rock Mechanics and Mining Sciences*, vol. 64, pp. 210–219, 2013.
[27] A. N. Antão, T. G. Santana, M. Vicente da Silva, and N. M. da Costa Guerra, "Passive earth-pressure coefficients by upper-bound numerical limit analysis," *Canadian Geotechnical Journal*, vol. 48, no. 5, pp. 767–780, 2011.
[28] D. Benmeddour, M. Mellas, R. Frank, and A. Mabrouki, "Numerical study of passive and active earth pressures of sands," *Computers and Geotechnics*, vol. 40, pp. 34–44, 2012.
[29] A. Locat, H. P. Jostad, and S. Leroueil, "Numerical modeling of progressive failure and its implications for spreads in sensitive clays," *Canadian Geotechnical Journal*, vol. 50, no. 9, pp. 961–978, 2013.
[30] Y.-p. Yin, B. Huang, X. Chen, G. Liu, and S. Wang, "Numerical analysis on wave generated by the qianjiangping landslide in three Gorges reservoir, China," *Landslides*, vol. 12, no. 2, pp. 355–364, 2015.
[31] Y. Zheng, C. Chen, T. Liu, H. Zhang, K. Xia, and F. Liu, "Study on the mechanisms of flexural toppling failure in anti-inclined rock slopes using numerical and limit equilibrium models," *Engineering Geology*, vol. 237, pp. 116–128, 2018.
[32] N. Li and Q.-h. Qian, "Four criteria of stability analysis and assessment of high rock slope," *Chinese Journal of Rock Mechanics and Engineering*, vol. 29, no. 9, pp. 1754–1759, 2010.
[33] H. Suwa, T. Mizuno, S. Suzuki, Y. Yamamoto, and K. Ito, "Sequential processes in a landslide hazard at a slate quarry in Okayama, Japan," *Natural Hazards*, vol. 45, no. 2, pp. 321–331, 2008.
[34] B. Leshchinsky, F. Vahedifard, H.-B. Koo, and S.-H. Kim, "Yumokjeong landslide: an investigation of progressive failure of a hillslope using the finite element method," *Landslides*, vol. 12, no. 5, pp. 997–1005, 2015.
[35] V. Gischig, G. Preisig, and E. Eberhardt, "Numerical investigation of seismically induced rock mass fatigue as a mechanism contributing to the progressive failure of deep-seated landslides," *Rock Mechanics and Rock Engineering*, vol. 49, no. 6, pp. 2457–2478, 2016.
[36] G. Prountzopoulos, P. Fortsakis, K. Seferoglou, F. Chrysochoidis, I. Vassilopoulou, and V. Perleros, "Assessment of failure mechanism and rehabilitation of a landslide within marly formations in NW Greece: from the site investigation to the geotechnical design," *Geotechnical & Geological Engineering*, vol. 32, no. 6, pp. 1485–1502, 2014.

[37] V. Kumar, V. Gupta, and I. Jamir, "Hazard evaluation of progressive Pawari landslide zone, Satluj valley, Himachal Pradesh, India," *Natural Hazards*, vol. 93, no. 2, pp. 1029–1047, 2018.

[38] A. Yerro, N. M. Pinyol, and E. E. Alonso, "Internal progressive failure in deep-seated landslides," *Rock Mechanics and Rock Engineering*, vol. 49, no. 6, pp. 2317–2332, 2016.

[39] O.-L. A. Kwok, P.-C. Guan, W.-P. Cheng, and C.-T. Sun, "Semi-Lagrangian reproducing kernel particle method for slope stability analysis and post-failure simulation," *KSCE Journal of Civil Engineering*, vol. 19, no. 1, pp. 107–115, 2015.

[40] F. Miao, Y. Wu, Y. Xie, F. Yu, and L. Peng, "Research on progressive failure process of Baishuihe landslide based on Monte Carlo model," *Stochastic Environmental Research and Risk Assessment*, vol. 31, no. 7, pp. 1683–1696, 2017.

[41] Y. F. Lu, L. P. Yang, and D. F. Liu, "A new joint constitutive model and several new methods of stability coefficient calculation of landslides," *Chinese Journal of Rock Mechanics and Engineering*, vol. 32, no. 12, pp. 2431–2438, 2013.

[42] Y. F. Lu, "Deformation and failure mechanism of slope in three dimensions," *Journal of Rock Mechanics and Geotechnical Engineering*, vol. 7, no. 2, pp. 109–119, 2015.